CLIMATOLOGY

An early Cambrian greenhouse climate

Thomas W. Hearing,[1,2]* Thomas H. P. Harvey,[1]* Mark Williams,[1]* Melanie J. Leng,[3,4]
Angela L. Lamb,[3] Philip R. Wilby,[2] Sarah E. Gabbott,[1] Alexandre Pohl,[5] Yannick Donnadieu[5]

The oceans of the early Cambrian (~541 to 509 million years ago) were the setting for a marked diversification of animal life. However, sea temperatures—a key component of the early Cambrian marine environment—remain unconstrained, in part because of a substantial time gap in the stable oxygen isotope ($\delta^{18}O$) record before the evolution of euconodonts. We show that previously overlooked sources of fossil biogenic phosphate have the potential to fill this gap. Pristine phosphatic microfossils from the Comley Limestones, UK, yield a robust $\delta^{18}O$ signature, suggesting sea surface temperatures of 20° to 25°C at high southern paleolatitudes (~65°S to 70°S) between ~514 and 509 million years ago. These sea temperatures are consistent with the distribution of coeval evaporite and calcrete deposits, peak continental weathering rates, and also our climate model simulations for this interval. Our results support an early Cambrian greenhouse climate comparable to those of the late Mesozoic and early Cenozoic, offering a framework for exploring the interplay between biotic and environmental controls on Cambrian animal diversification.

INTRODUCTION

The oxygen isotope ($\delta^{18}O$) composition of fossil biominerals is one of the most widely used proxies for investigating ancient environments and is particularly useful as a deep time paleothermometer (1). The most widespread $\delta^{18}O$ records come from analyses of calcium carbonate (2–4) and calcium phosphate (5–7) marine shelly fossils. However, although a near-continuous $\delta^{18}O$ record exists back to the Early Ordovician epoch, 485 million years (Ma) ago (1, 6), there is a substantial early Phanerozoic data gap that covers the interval of the Cambrian explosion, when the oldest identifiable fossils of most of the animal phyla appear in the rock record (8). This gap exists because phosphatic euconodonts with diagenetically robust hyaline crown tissues (9) are absent below uppermost Cambrian strata, whereas most calcareous fossils in these rocks have been demonstrably diagenetically altered (1, 4). An alternative source of Cambrian oxygen isotope data is therefore needed to quantitatively assess the state of the early Cambrian climate, which has so far only been qualitatively interpreted as a greenhouse interval (8, 10, 11). We propose that "small shelly fossils" (SSFs) are a potential new source of $\delta^{18}O$ data that could help constrain Cambrian marine environments.

SSFs comprise the skeletal elements of a diverse range of early biomineralizing animals that produced siliceous, calcareous, or phosphatic skeletons. Although many SSFs are preserved in secondary (diagenetic) phosphate (12), some are suggested to retain an original biophosphatic composition (13). To avoid sampling secondarily phosphatized specimens, we targeted fossils from the Comley Limestones, Shropshire, UK (fig. S1). These rocks are notable for yielding arthropods with limited (and very early) secondary phosphatization of soft anatomy but lack evidence for phosphatic replacement of original shell material (14). The Comley Limestones were deposited under normal marine conditions beneath the well-mixed waters of a shallow sea (15), approximately 65°S to 70°S on the peri-Gondwanan microcontinent Avalonia (16) between 514.45 ± 0.36 and 509.10 ± 0.22 Ma ago (17).

To ensure that isotope data recovered from the phosphatic SSFs reflect a Cambrian paleoenvironmental signal rather than later diagenetic conditions, we restricted our analyses to taxa known to have produced phosphatic skeletons based on phylogenetic and geological criteria (13). These included linguliformean brachiopods, which have well-known extant relatives, and the robust, thick-walled benthic tubular microfossil *Torellella*. We assembled taxon-specific samples for bulk isotope analysis comprising tens to a few hundred individual specimens and separated them according to their visual quality of preservation (fig. S2). Representative specimens from each bulk subset were subjected to a rigorous protocol to assess the preservation of biogenic phosphate. We could consistently distinguish subsets of pristine and altered SSFs using optical microscopy, confirmed by combining high-resolution scanning electron microscopy (SEM) and energy dispersive x-ray (EDX) spectroscopy to assess micro- and ultrastructural preservation and the distribution of diagenetically sensitive elements (see Materials and Methods). In particular, brachiopod specimens taken from pristine subsets were found to have compact laminae comprising phosphate spherules tens of nanometres in diameter, whereas the compact laminae of specimens taken from altered subsets were recrystallized as micrometer-scale phosphate prisms (Fig. 1). To help define a $\delta^{18}O$ diagenetic gradient, we also analyzed an early diagenetic phosphate hardground, which likely formed at or close to the sediment-water interface, soon after deposition, from pore waters in communication with the overlying ocean (see Materials and Methods).

RESULTS AND DISCUSSION

Bulk oxygen isotope analyses (see Materials and Methods and data S1) of pristine phosphatic microfossils (five samples of linguliformean brachiopods and two of *Torellella*) yielded $\delta^{18}O_{phos}$ values of +13.9 to +15.2 per mil (‰) Vienna standard mean ocean water (VSMOW). In contrast, three linguliformean brachiopod samples, identified a priori as being affected by diagenetic alteration, yielded lighter values of +13.3 to +14.3‰ (Fig. 2). Samples of sedimentary phosphate from an early diagenetic phosphatic hardground, in situ and as a rip-up clast, yielded still lighter $\delta^{18}O_{phos}$ values ranging from +12.8 to +14.0‰.

In paired analyses of linguliformean brachiopods from the same sample, identified during our preanalysis screening as preserving either
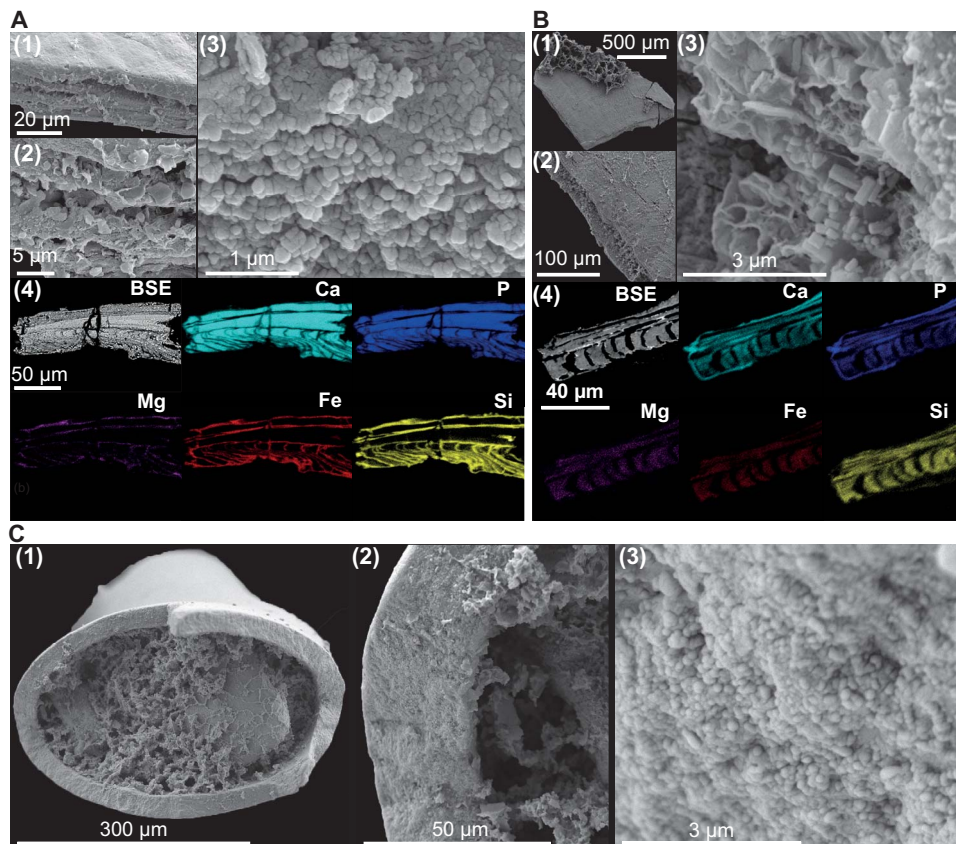
Fig. 1. Preservation of linguliformean brachiopods and *Torellella* from the Comley Limestones. (**A**) SEM and EDX analyses of pristine brachiopods preserve alternating compact and porous phosphatic laminae [(1) and (2)]; compact laminae comprise densely packed phosphatic spherules (3). Diagenetically sensitive elements, particularly Fe and Mg, are restricted to porous laminae (4). BSE, backscattered electron image. (**B**) SEM and EDX analyses of altered brachiopods may preserve laminar microstructure, but compact laminae phosphate has recrystallized to micrometer-scale prismatic crystals (3). Diagenetically sensitive elements indicative of alteration are found throughout altered specimens (4). (**C**) Pristine *Torellella* specimens comprise densely packed phosphatic spherules a few tens of nanometers in diameter (3).

pristine or demonstrably altered phosphate, the pristine brachiopods consistently yielded heavier $\delta^{18}O_{phos}$ than their diagenetically altered counterparts, by +0.3 to +1.0‰. The close correspondence of the $\delta^{18}O_{phos}$ of diagenetically altered brachiopods (+13.3 to +14.3‰) to those of the phosphate hardground (+12.8 to +14.0‰) suggests that these altered SSFs may record early diagenetic conditions or at least have followed a similar diagenetic pathway as the hardground. In contrast, pristine *Torellella* samples yielded $\delta^{18}O_{phos}$ values of 14.6 to 14.7‰, comparable to the pristine brachiopods (+13.9 to +15.2‰) and heavier values than those from the diagenetically altered brachiopods and the hardground samples. Most *Torellella* specimens were identified as pristine, and altered *Torellella* specimens were too scarce to assemble samples for bulk analysis (see Materials and Methods).

In situ secondary ion mass spectrometry (SIMS) analysis shows that oxygen isotopic preservation varies in the same manner as bulk elemental composition within individual brachiopod specimens (see Materials and Methods, fig. S3, and data S2). SIMS analysis consistently distinguishes between the $\delta^{18}O$ values of compact and porous laminae, with compact laminae consistently heavier, by at least approximately 2‰, than porous laminae in the same specimen (Fig. 2). Bulk $\delta^{18}O_{phos}$ values approximate to those of the compact laminae, likely because of the proportionately small contribution of the phosphate in the porous laminae to the total volume of shelly material analyzed (*18*, *19*). The systematic

offset between the heavier values in the bulk $\delta^{18}O_{phos}$ and lighter values from in situ SIMS analyses (Fig. 1) is likely due to the incorporation of all oxygen isotope species in a SIMS analysis spot [including the high proportion of structural carbonate in biogenic apatite (*19*)], compared with only phosphate-bound oxygen (PO_4^{3-}) measured by the trisilver bulk phosphate method. Because phosphate-oxygen temperature equations are based on trisilver $\delta^{18}O_{phos}$ analyses (*7*, *20–22*), bulk $\delta^{18}O_{phos}$ analyses are likely the most robust paleoenvironmental data from SSFs, with SIMS analyses providing critical information on intrasample variability and preservation.

Isotopic composition of Cambrian seas

Selected SSFs from the Comley Limestones, screened to identify and exclude specimens unduly affected by diagenetic alteration, give $\delta^{18}O_{phos}$ values that reflect shallow marine conditions on early Cambrian Avalonia. The $\delta^{18}O_{phos}$ data incorporate signals from the oxygen isotopic composition of contemporaneous sea water ($\delta^{18}O_{sw}$), the temperature of the water in which the animal lived, and biological fractionation ("vital effects"). The convergence of phosphate oxygen isotope temperature equations based on both marine invertebrate and nonmammalian marine vertebrate biominerals indicates that phosphate oxygen vital effects are small in comparison with analytical uncertainty (*21*). The impact of any vital effects in the phosphate oxygen
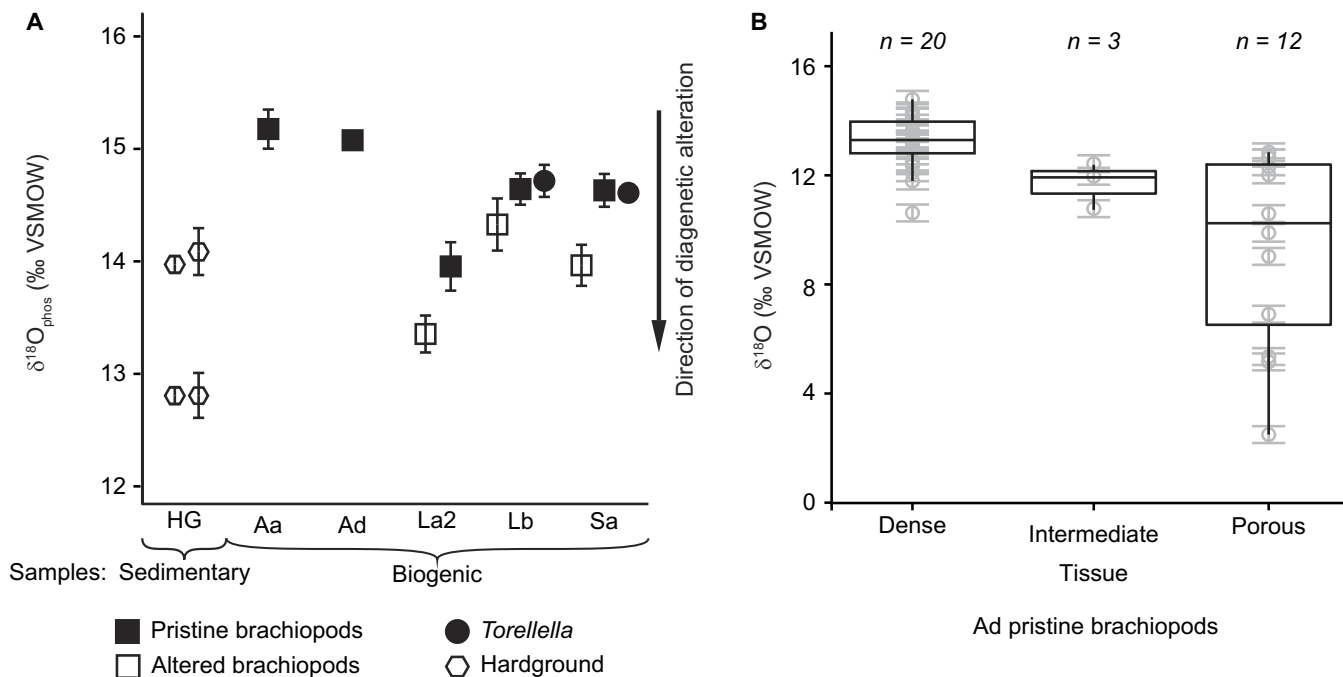
Fig. 2. Early Cambrian δ18Ophos data from SSFs from the Comley Limestones. (**A**) In bulk analyses, altered subsets are isotopically lighter than the pristine counterparts from the same sample. Sample labels follow Table 1; error bars of 1 SD; δ18Ophos indicates trisilver phosphate analysis in which only phosphate oxygen isotopes were measured. (**B**) In situ (SIMS) data from linguliformean brachiopod specimens (sample Ad) show that porous laminae are consistently isotopically lighter than compact laminae. See data S1 and fig. S3. Box plots display the median and first and third quartiles, with the whiskers extending up to 1.5 times the interquartile range. All isotope data are reported relative to VSMOW.

isotope system is incorporated within the uncertainty of the empirically derived phosphate oxygen temperature (Eq. 1) (*22*)

$$T(°C) = (117.4 ± 9.5) − [(4.50 ± 0.43)*(δ^{18}O_{phos} − δ^{18}O_{sw})] \quad (1)$$

However, an estimate of $δ^{18}O_{sw}$ is still required. Local $δ^{18}O_{sw}$ is a function of the $δ^{18}O_{sw}$ of the global ocean average value, the local influence of freshwater input, and the regional precipitation-evaporation (P-E) balance (*23*). Secular variability of the global ocean $δ^{18}O$ reservoir, other than ice volume effects of ~1‰, is often disregarded in deep time paleoclimate studies (*5*, *6*) because of the potential buffering effect of balanced hot and cold hydrothermal alteration processes (*24*)—a view that has found some support from the emerging field of carbonate clumped isotopes (*25*–*28*). However, an invariant global ocean $δ^{18}O$ reservoir is at odds with the long-term carbonate, phosphate, and silica records, which all show comparable nonlinear secular trends in $δ^{18}O$ values (*2*, *4*, *5*, *29*, *30*). Over the Phanerozoic eon, this trend is thought to have shifted the $δ^{18}O$ value of the global ocean reservoir from approximately −6‰ in the early Cambrian to the heavier modern values of −1 to 0‰ (*2*, *4*, *30*). The $δ^{18}O_{sw}$ secular trend is further supported by similar magnitude trends derived from numerical modeling, with a substantial amount of this shift occurring in the early part of the Phanerozoic eon (*31*, *32*).

Our new data support a secular trend in the global ocean $δ^{18}O$ reservoir and extend the biomineral isotope evidence for this trend back into the early Cambrian (Fig. 3 and data S3). We therefore suggest that paleoenvironmental $δ^{18}O$ studies in deep time should detrend raw data before making paleoenvironmental interpretations of temperature or

ice volume change to account for this secular variation. To avoid the circularity of inferring both $δ^{18}O_{sw}$ and temperature from our data, we use preexisting whole-rock data (*4*) and geochemical modeling (*31*, *32*) to infer that global average early Cambrian $δ^{18}O_{sw}$ was approximately −6‰.

In addition to secular variability, we account for latitudinal P-E effects on local $δ^{18}O_{sw}$ in our temperature calculations—an important factor in paleoclimate research on more recent intervals but which is not usually considered in Paleozoic studies (*26*–*28*, *33*). Latitudinal P-E effects in modern oceans can be substantial, with surface $δ^{18}O_{sw}$ values ranging from −7.7 to +2.5‰ (*34*), although most of the global ocean is within ±1.5‰ of the global average (*23*, *34*, *35*). Isotope-enabled climate models for the early Cenozoic greenhouse climate suggest that the $δ^{18}O_{sw}$ distribution was similar to that of modern oceans, with perhaps slightly increased variability driven by an enhanced hydrological cycle (*36*, *37*). Given the well-connected position of Avalonia to the global ocean in the early Paleozoic (see Materials and Methods and fig. S1) and the range of $δ^{18}O_{sw}$ at comparable high southern latitudes in both the current icehouse and early Cenozoic greenhouse climate states (*34*–*37*), we use a conservative estimate of a −0.5‰ deviation from the Cambrian global average of −6‰ to give a $δ^{18}O_{sw}$ value of −6.5‰.

Cambrian sea surface temperatures
Because the Comely Limestones were deposited in a shallow marine setting (*15*), we can interpret our isotope data as reflecting sea surface, rather than deep marine, conditions. Using the phosphate oxygen temperature (Eq. 1) (*22*) with a $δ^{18}O_{sw}$ value of −6.5‰, we reconstruct sea surface temperatures (SSTs) of 20° to 25°C for the Comley Limestones (Table 1). This is within the range of high-latitude temperatures of more
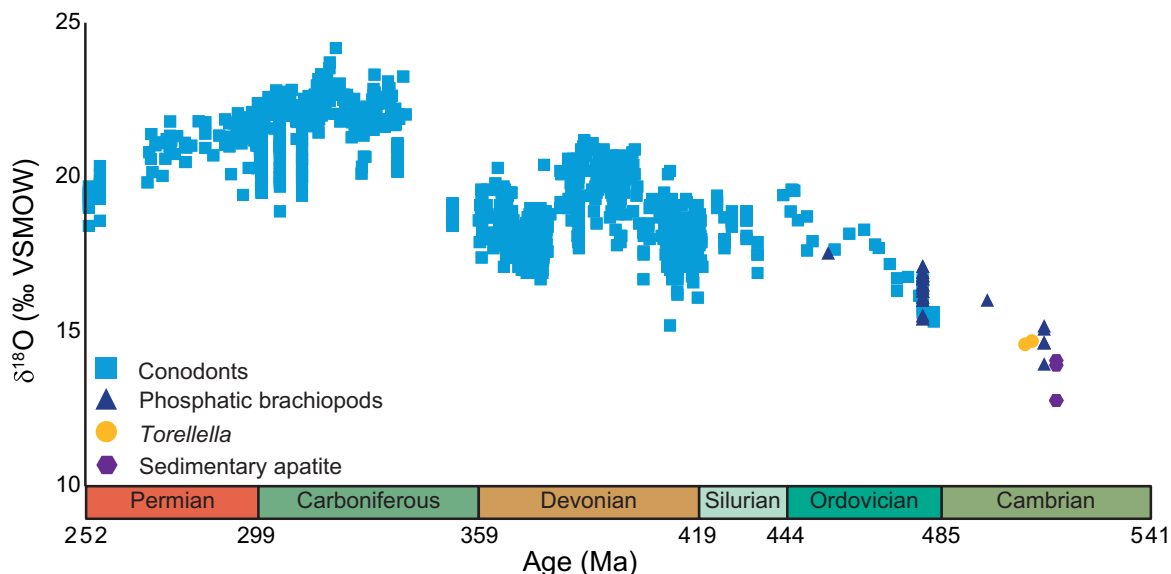
Fig. 3. The Paleozoic phosphate $\delta^{18}O$ record. Conodonts, blue squares; well-preserved linguliformean brachiopods, dark blue triangles; well-preserved *Torellella* samples, yellow circles; phosphate hardground data, purple hexagons). This trend is most pronounced in the earlier part of the Paleozoic. Data span a range of paleolatitudes and water depths. Our Cambrian data are essentially contemporaneous at approximately 513 Ma ago; for clarity, *Torellella* and phosphate hardground points have been shifted slightly on the age axis. All values are relative to VSMOW. See data S3.

Table 1. Bulk (trisilver phosphate) $\delta^{18}O_{phos}$ data from the Comley Limestones and SSTs exploring the influence of different values for $\delta^{18}O_{sw}$. Temperatures calculated from Eq. 1 (22). T_1 $\delta^{18}O_{sw} = -6.5‰$, the most reasonable value; T_2 $\delta^{18}O_{sw} = -6‰$, assumes no latitudinal P-E effects; T_3 $\delta^{18}O_{sw} = -1‰$, the most commonly used Paleozoic value; T_4 $\delta^{18}O_{sw} = -8‰$, incorporating the maximum likely latitudinal P-E effect of $-2‰$. Temperature uncertainty (2 SD T_1) calculated from $\delta^{18}O$ measurement SDs, assuming that $\delta^{18}O_{sw} = -6.5‰$. See data S1.

Sample	Triplicate mean $\delta^{18}O_{phos}$ (‰ VSMOW)	Triplicate 1 SD (‰ VSMOW)	T_1 (°C)	T_2 (°C)	T_3 (°C)	T_4 (°C)	2 SD T_1 (°C)
Pristine brachiopods							
Aa-Br-L	15.17	0.18	20	22	45	13	1.6
Ad-Br-L	15.06	0.03	20	23	45	14	0.3
La2-Br-L	13.93	0.22	25	28	50	19	2.0
Lb-Br-L	14.63	0.14	22	25	47	16	1.3
Sa-Br-L	14.62	0.15	22	25	47	16	1.3
Pristine *Torellella*							
Lb-To-To	14.70	0.14	22	24	47	15	1.3
Sa-To-To	14.59	0.07	22	25	47	16	0.6
Altered brachiopods							
La2-Br-D	13.33	0.17	28	30	53	21	1.5
Lb-Br-D	14.31	0.23	24	26	49	17	2.1
Sa-Br-D	13.94	0.18	25	28	50	19	1.7
Sedimentary phosphate							
HG-A	13.95	0.05	25	28	50	19	0.5
HG-A-DC	14.07	0.21	25	27	50	18	1.9
HG-B	12.77	0.09	31	33	55	24	0.8
HG-B-DC	12.78	0.20	31	33	55	24	1.8

recent greenhouse intervals in Earth's history (Fig. 4 and data S4), such as those of the late Mesozoic and early Cenozoic (38–41).

Repeating our calculations assuming the ice-free Cenozoic value of −1‰ for $\delta^{18}O_{sw}$ typically used in Paleozoic paleoclimate studies (5, 6), rather than −6.5‰, our isotopic temperatures would shift from ~45° to 50°C (Table 1). This is unrealistic for high-latitude SSTs because they approach or exceed the lethal temperature limits for many marine animals, including brachiopods (42). We note that our $\delta^{18}O_{phos}$ values are similar to those derived from well-preserved conodonts from the Tremadocian (Early Ordovician) of northern Gondwana (5) and Laurentia (6), which provide SST estimates of 40° to 44°C, assuming a $\delta^{18}O_{sw}$ value of −1‰, albeit for lower latitudes. However, a recent paleoclimate modeling study encompassing the Early Ordovician epoch predicts much lower sea temperatures for the paleogeographic positions of these conodont $\delta^{18}O$ data (43). Sea temperature estimates of 27° to 30°C, in much closer agreement with general circulation model (GCM) estimates (43), are obtained when a detrended Early Ordovician global ocean average $\delta^{18}O_{sw}$ value of −4‰ (32) is used. Detrending the conodont $\delta^{18}O_{phos}$ record to account for the observed $\delta^{18}O$ secular trend (2, 4, 29) improves data-model comparison in early Paleozoic climate studies (43), providing further confidence in our $\delta^{18}O_{sw}$ value.

Paleoclimate implications

The characteristically warm high-latitude temperatures of greenhouse climate intervals, particularly noticeable in Mesozoic and Cenozoic paleotemperature proxy records (38–41), are consistent with our reconstructed SSTs (Fig. 4). Early Cambrian geological data generally support interpretations of a greenhouse climate state lacking permanent polar ice sheets, with evaporite and calcrete deposits spanning a wide paleolatitudinal range (10), the deposition of tropical soils (laterites) at high paleolatitudes (44), and a maximum of continental weathering rates over the past 900 Ma (11).

However, there may be some evidence for glaciation at high paleolatitudes (Avalonia) or even mid-paleolatitudes (Baltica) during the early Cambrian (45, 46). Imprecise age constraints have hindered integration of these possible cold-climate deposits into the international stratigraphic framework, with some age estimates ranging from late Neoproterozoic to Early Ordovician. However, the likelihood is that these deposits (45, 46) are of earliest (pretrilobitic) Cambrian or late Neoproterozoic age. Because our data from Cambrian Age 4 suggest climatic conditions that preclude even polar land ice at low altitude, it seems likely that any glacial activity was restricted to the earliest Cambrian or to short duration icehouse intervals.

To further investigate the viability of our temperature estimates, we ran new GCM simulations of the early Cambrian climate (Fig. 5 and fig. S4) using the Fast Ocean Atmosphere Model (FOAM) (47)—a coupled ocean-atmosphere GCM that has recently been applied to interrogate other questions about early Paleozoic climates (43, 48). The GCM simulations found good agreement with our new data for CO_2-equivalent forcing of 32 times preindustrial atmospheric levels (PALs; 280 parts per million). This greenhouse gas forcing is in line with Cambrian pCO_2 (partial pressure of CO_2) estimates from GEOCARB suite of models (49). Both the data- and GCM-derived temperatures are comparable
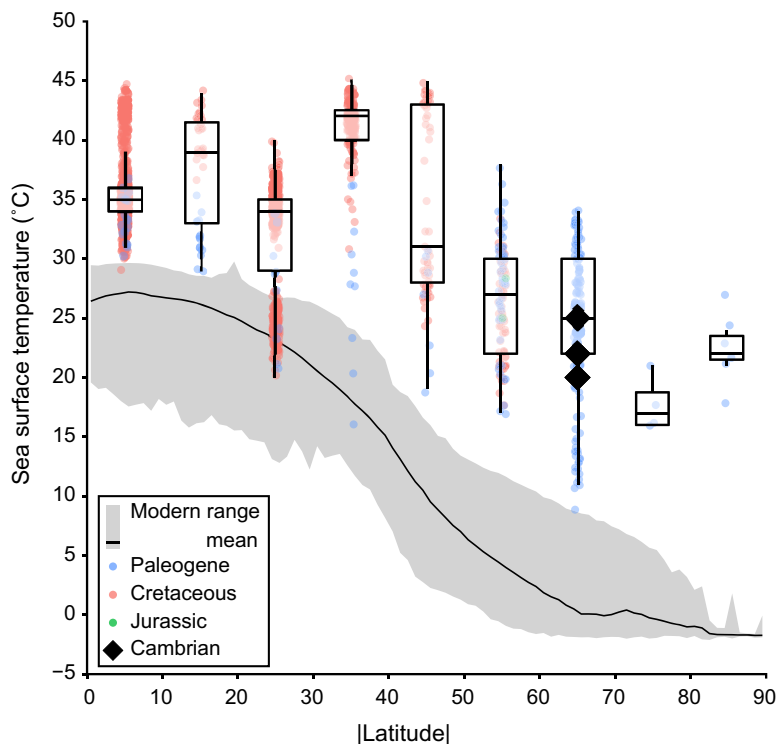
Fig. 4. Cambrian isotopic SSTs in the context of Mesozoic and early Cenozoic greenhouse climate states. Cambrian data (black diamonds) from the $\delta^{18}O_{phos}$ values of pristine SSF samples from the Comley Limestones. Data are plotted in 10° bins of the modulus of paleolatitude to illustrate latitudinal temperature variation irrespective of paleocontinental configuration. Plotted point data summarized in box plots displaying the median and first and third quartiles, with the whiskers extending up to 1.5 times the interquartile range. Cretaceous data, Cenomanian to Turonian; Paleogene data, Paleocene to Eocene. For references and literature data, see data S4. The modern latitudinal mean (black line) and range (gray envelope) data from the 2013 World Ocean Atlas 1° resolution data set (60).
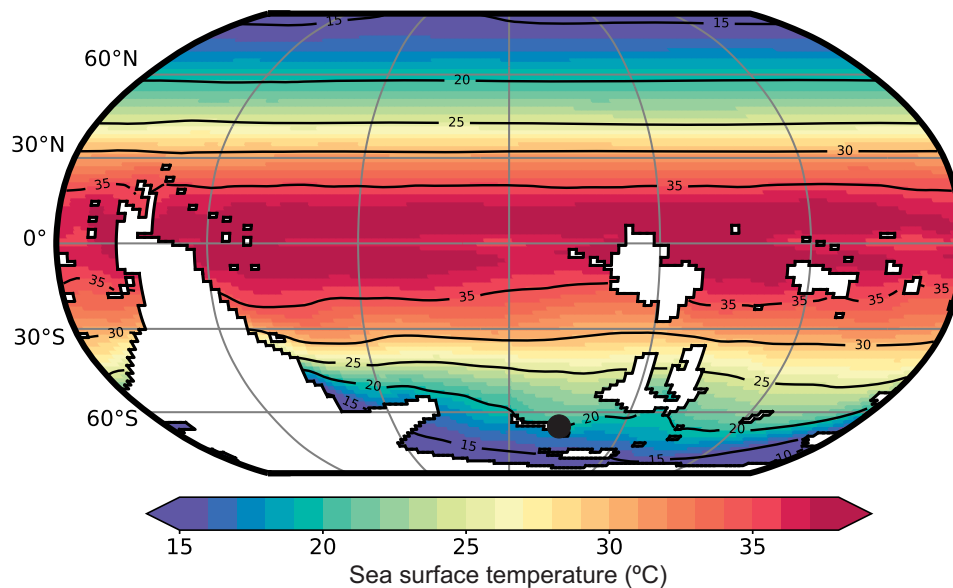
Fig. 5. Early Cambrian mean annual SSTs, modeled by the FOAM GCM. The simulation was run under present-day orbital configurations with a CO_2-equivalent greenhouse gas forcing of 32 PAL (see Materials and Methods and fig. S4). Black spot marks the position of our $\delta^{18}O_{phos}$ data on Avalonia.

to late Mesozoic and early Cenozoic greenhouse conditions (Fig. 4) (*38–41*).

Overall, our new data provide the first quantitative constraints on early Cambrian climate, corroborating qualitative geological data and geochemical arguments that also support interpretations of this as a greenhouse world. Our new data fill an extensive time gap in the paleotemperature record of the beginning of the Phanerozoic eon and provide environmental context to a time when the animal-rich marine ecosystems of the Phanerozoic were first evolving. Using quantitative data to inform environmental and climate models will enable more rigorous interrogation of first-order hypotheses surrounding the ecological revolutions of the Cambrian Period, and these data can be recovered from globally widespread phosphatic Cambrian microfossils.

MATERIALS AND METHODS
Materials
The Comley Limestones
The Comley Limestones were deposited in a shallow sea (*15*) at ~65°S to 70°S on the peri-Gondwanan microcontinent Avalonia (*16*) between 514.45 ± 0.36 and 509.10 ± 0.22 Ma ago (fig. S1) (*17*). This fossiliferous and highly condensed limestone unit is less than 2 m thick, with five lithostratigraphic units (Ac_2 to Ac_5 and Ad) recognized on the basis of their petrographic and paleontological characteristics and separated by erosional disconformities that represent depositional hiatuses (*15*). Glauconite clasts and laminated iron-manganese nodules are common throughout the succession. The horizons are all more-or-less sandy limestones, with detrital mineral abundance and faunal composition varying throughout the succession. The abundance of glauconite, laminated iron-manganese nodules, evidence for erosion and condensation, and the typically stenohaline trilobitic fauna indicates that there was no major freshwater (riverine) influence. There was deposition characteristic of normal marine conditions in the Welsh Basin throughout much of the Cambrian, Ordovician, and Silurian (*50*), and its peri-Gondwanan position close to the passive margin of the Iapetus Ocean during the Cambrian Period

(*16*) suggests that it was well connected to the global ocean. The Comley Limestones are considered to have been deposited in an energetic shallow marine environment (*15*) that was unlikely to have been subjected to a seasonal thermocline.

Microfossil processing
Blocks of the Comley Limestones were macerated in buffered (10 to 15%) acetic acid using a standard extraction protocol, modified after Jeppsson *et al.* (*51*), that is not known to affect $\delta^{18}O$ values (*9*). Heavy liquid separation, which is commonly used to concentrate microfossils within an acid residue but is known to affect $\delta^{18}O_{phos}$ values (*9*), was not used. Acetic acid residues were collected between 1000- and 125-μm sieves and thoroughly rinsed with deionized water before being gently dried in an oven ($T < 50°C$). The residues were subsequently examined using a binocular microscope, and fossil specimens were picked out with a brush and deionized water. SSFs were assembled into 30-mg taxon-specific bulk samples, with each sample comprising several tens to a few hundred individual specimens.

Specimens were assembled into "pristine" and "altered" samples based on their appearance under optical microscopy. Pristine brachiopod specimens had a translucent light-brown appearance under reflected light, whereas altered specimens were opaque and appeared very dark brown to black (fig. S2). Specimens intermediate between these end-member states were excluded from further analysis. The vast majority of *Torellella* specimens were deemed pristine: light blue-gray in color, thick-walled, and with visible growth structures both within the tube walls and on the exterior surface. Although altered *Torellella* specimens exist (bleached white or black in color and with tube walls typically thin with no internal or external differentiation), no lithological sample yielded sufficient of these for bulk isotope analysis. The actual preservation state of samples was confirmed following the protocol outlined below.

Microfossil preservation
Because it was not possible to assess the preservation of every fossil in a bulk isotope sample, individual representative specimens were taken from bulk samples and examined to determine the typical preservation of each sample. Fractured surfaces of individual specimens were

examined using high-magnification SEM to investigate the extent of recrystallization or overgrowth by diagenetic phosphate. Polished cross sections of individual specimens embedded in epoxy resin were examined using EDX spectroscopy to investigate the extent of chemical alteration and particularly the distribution of any such alteration within individual specimens.

The shells of modern linguliformean brachiopods comprised alternating dense layers of biophosphate (compact laminae) and organic-rich layers with much less biophosphate (porous laminae of various morphologies). The compact laminae, which constituted most of the biomineralized material, were composed of densely packed calcium phosphate spherules measuring from tens to a few hundred nanometers in diameter (18). We identified these submicrometer-scale phosphatic spherules in the compact laminae of specimens taken from pristine bulk samples (Fig. 1 and fig. S1). We also found these submicrometer-scale phosphatic spherules in specimens taken from pristine samples of the tubular SSF *Torellella* (Fig. 1). Specimens from samples identified as diagenetically altered showed recrystallization of these spherules, forming micrometer-scale phosphatic prisms (Fig. 1). These very small crystallite sizes, where microstructures are otherwise well preserved, may simply reflect solid-state recrystallization with no or minimal isotopic exchange because phosphate oxygen isotopes are known to be robust to low-temperature non–microbially mediated recrystallization (52). Secondary phosphatization was restricted to apatite overgrowths protruding into the porous laminae of specimens taken from samples of altered brachiopod samples. Overgrowths were also observed in some *Torellella* specimens, although where present, this was apparent under optical microscopy as bulges formed on the surfaces of these specimens wherever overgrowths had formed. *Torellella* specimens with these bulges were excluded from isotope analyses. In the most severely altered brachiopod specimens, all internal microstructure was lost, with the specimens being preserved as crude (blocky) outlines only.

Individual specimens from pristine and altered samples were embedded in epoxy resin and cured under pressure (approximately 2 bar) before being ground and polished with silicon carbide paper, diamond paste, and γ-alumina, before being thoroughly rinsed with ethanol and deionized water. EDX analyses of these specimens enabled us to map element distributions across different biological domains (compact and porous laminae). In brachiopod specimens taken from pristine samples, we found that elements indicative of alteration (most commonly, Fe, Mg, and Si) were restricted to porous laminae and were excluded from compact laminae (Fig. 1). In EDX analyses of specimens taken from altered samples, we found that these elements pervade the brachiopod compact laminae, where we had already observed prismatic phosphate recrystallization (Fig. 1). Having confirmed these preservation states with detailed SEM-EDX investigations, we determined that it was possible to separate pristine and altered specimens into bulk isotope samples using optical microscopy (fig. S2).

Phosphatic hardground

Sedimentary phosphate samples were also taken for bulk isotope analysis to provide a $\delta^{18}O$ diagenetic gradient. These were acquired by microdrilling approximately 30 mg of powder from an irregular phosphatic hardground (HG-A) horizon in the lower part of the Comley Limestones and from a phosphatic pebble (HG-B) a few centimeters above the hardground. The in situ hardground is up to 3 cm deep, with an angular upper surface, and separates two distinct lithologies: an underlying trilobite-rich sandy limestone and an overlying glauconite-rich sandy limestone with few fossils. The overlying glauconite-rich

unit also contains subrounded to angular phosphatic pebble-sized clasts. In places, the uppermost part of the hardground includes laminae of glauconite and quartz clasts.

Petrographic observations, including the lithological differences between the underlying and overlying units, the irregular upper surface, the preservation of calcareous fossils between the phosphate groundmass, and the fine glauconite and quartz laminae near the top of the horizon, suggested an early diagenetic origin of the phosphate, with occasional interruption of phosphate precipitation at the sediment-water interface and, ultimately, exposure of the hardground on the sea bed. Phosphate clasts were incorporated into the horizon above the hardground and were interpreted as deriving from the hardground during its exposure on the sea bed after its formation.

Methods
Bulk isotope analyses

All $\delta^{18}O$ values were reported with respect to VSMOW. Bulk isotope data were obtained from 30-mg fossil samples, with each sample comprising several tens of individual specimens, treated to solubilize PO_4 anions and precipitated as silver phosphate [adapted after O'Neil et al. (53)] at the Natural Environment Research Council (NERC) Isotope Geoscience Facilities (NIGF). Samples of microfossils were crushed using a glass rod, cleaned in concentrated hydrogen peroxide for 24 hours to remove organic material, and subsequently evaporated to dryness. The samples were then dissolved in 2 M HNO_3 and transferred to clean polypropylene test tubes. Each sample was then treated with 2 M KOH for neutralization and 2 M HF to remove calcium from the solution by precipitation of calcium fluoride. The samples were then centrifuged, and the supernatant was added to beakers containing ammoniacal silver nitrate solution and heated gently to precipitate silver phosphate. The silver phosphate was filtered, rinsed, dried, and weighed into silver capsules for analysis. Oxygen isotope measurements on each sample were analyzed in triplicate by continuous flow isotope ratio mass spectrometry (54). Analysis was via a high-temperature conversion elemental analyzer coupled to a Delta Plus XL isotope ratio mass spectrometer via a ConFlo III interface (Thermo Finnigan). The reference material B2207 (silver phosphate, Elemental Microanalysis) has an accepted value of 21.70‰, and the reproducibility of B2207 during this set of analyses was better than ±0.15 (1σ). All $\delta^{18}O$ analyses were performed in triplicate, and the average SD of the triplicates was ±0.15‰.

Ion microprobe analyses

In situ SIMS analyses were conducted at the Edinburgh Ion Microprobe Facility (EIMF). For SIMS analysis, specimens were embedded under pressure (2 bar) in epoxy resin within 5 mm of the center of the block and around a central Durango apatite standard. Sample blocks were prepared using diamond grinding compounds, followed by diamond and alumina polishing compounds. Sample blocks were treated for 24 hours with H_2O_2 to remove organic matter from the embedded fossils. Surface reimpregnation, with minimal regrinding and polishing, was used to ensure a smooth and flat surface before gold coating for SIMS analysis.

SIMS analyses were made using the CAMECA IMS-1270 ion microprobe. A primary beam of Cs^+ ions at ~5 nA was focused to a 30-μm-diameter spot on the sample block surface. Secondary ions were extracted at −10 kV, with ^{16}O [~2 × 10^9 counts/s (cps)] and ^{18}O (~4 × 10^6 cps) monitored simultaneously on dual Faraday cups (L'2 and H'2). Each analysis began with 50-s presputtering time, followed by automatic secondary beam and entrance slit centring, before data collection in two 10-cycle blocks. Each SIMS run began with 10 Durango

analyses, followed by alternating analysis sets of five unknowns (samples) and five standards (Durango apatites), dropping to three standards when beam stability was good. Linear regressions were applied to each analysis run to correct for instrument drift. Mean external precision was derived from the SD of Durango analyses following linear regression corrections for long-term (session duration) drift. This value was reported for each unknown (sample) analysis and ranged from ±0.11 to 0.41‰. The Durango apatite standards were fragments of a larger crystal, supplied by EIMF, whose isotopic composition ($\delta^{18}O_{phos}$, +8.7‰) was independently verified by trisilver phosphate analysis at NIGF before this project began.

Climate modeling

We used the three-dimensionally coupled ocean-atmosphere FOAM version 1.5 (47) that was widely applied to deep time paleoclimate studies (43, 48, 55, 56). The atmospheric module is a parallelized version of the National Center for Atmospheric Research Community Climate Model 2 (CCM2), upgraded to include radiative and hydrologic physics from CCM3 version 3.2. We ran the atmospheric module with R15 spectral resolution (4.5° × 7.5°) and 18 vertical levels. The ocean module was the higher-resolution Ocean Model version 3, a 24-level z-coordinate ocean GCM giving 1.4° × 2.8° resolution on a regular longitude-latitude grid. The coupled model had no flux corrections, and its short turn-around time allowed millennial-scale integration.

We used the Cambrian continental configuration from BugPlates for 510 Ma ago (57). In the absence of land plants, the land surface was defined as a rocky desert (albedo, 0.24; modified by snow, if present). The solar luminosity was decreased by 4.3 % compared to its present value (1368 W m^{-2}) (58), and orbital parameters were maintained constant to the present-day configuration. The pCO_2 was fixed at 32 PALs (59), and concentrations of other greenhouse gases were kept to the present-day level so that the imposed radiative forcing must be considered a CO_2 equivalent that may include some contribution of other greenhouse gases such as methane. The simulation was initialized using a warm ice-free ocean and a uniform salinity of 35‰. We integrated the model for 2000 years to reach deep-ocean equilibrium. During the last 100 years of the simulation, there was no apparent drift in the upper ocean and <0.01°C change in deep ocean (−3700 m) temperature. The last 50 years of the model run were used to build the climatology files used for analysis.

SUPPLEMENTARY MATERIALS

Supplementary material for this article is available at http://advances.sciencemag.org/cgi/content/full/4/5/eaar5690/DC1

fig. S1. Paleogeographic and stratigraphic setting of the Comley Limestones (Avalonia, Cambrian Series 2).

fig. S2. Examples of pristine and altered brachiopod and *Torellella* specimens.

fig. S3. Box plots of ion microprobe (SIMS) data collected from pristine linguliformean brachiopods by tissue sampled.

fig. S4. Global SST contour plots produced by early Cambrian FOAM GCM simulations for CO_2-equivalent forcing of 32 PALs (see Materials and Methods).

data S1. Triplicate trisilver phosphate isotope measurements.

data S2. Processed ion microprobe (SIMS) data.

data S3. Paleozoic phosphate $\delta^{18}O$ data used to produce Fig. 3.

data S4. Paleotemperature data used to produce Fig. 4.

References (61–124)

REFERENCES AND NOTES

1. E. L. Grossman, Oxygen isotope stratigraphy, in *The Geologic Time Scale*, F. M. Gradstein, J. G. Ogg, M. Schmitz, Eds. (Elsevier, 2012), pp. 181–206.

2. J. Veizer, D. Ala, K. Azmy, P. Bruckschen, D. Buhl, F. Bruhn, G. A. F. Carden, A. Diener, S. Ebneth, Y. Godderis, T. Jasper, C. Korte, F. Pawellek, O. G. Podlaha, H. Strauss, $^{87}Sr/^{86}Sr$, $\delta^{13}C$ and $\delta^{18}O$ evolution of Phanerozoic seawater. *Chem. Geol.* **161**, 59–88 (1999).

3. J. Zachos, M. Pagani, L. Sloan, E. Thomas, K. Billups, Trends, rhythms, and aberrations in global climate 65 Ma to present. *Science* **292**, 686–693 (2001).

4. J. Veizer, A. Prokoph, Temperatures and oxygen isotopic composition of Phanerozoic oceans. *Earth Sci. Rev.* **146**, 92–104 (2015).

5. D. Bassett, K. G. Macleod, J. F. Miller, R. L. Ethington, Oxygen isotopic composition of biogenic phosphate and the temperature of Early Ordovician seawater. *PALAIOS* **22**, 98–103 (2007).

6. J. A. Trotter, I. S. Williams, C. R. Barnes, C. Lécuyer, R. S. Nicoll, Did cooling oceans trigger Ordovician biodiversification? Evidence from conodont thermometry. *Science* **321**, 550–554 (2008).

7. E. Pucéat, M. M. Joachimski, A. Bouilloux, F. Monna, A. Bonin, S. Motreuil, P. Morinière, S. Hénard, J. Mourin, G. Dera, D. Quesne, Revised phosphate–water fractionation equation reassessing paleotemperatures derived from biogenic apatite. *Earth Planet. Sci. Lett.* **298**, 135–142 (2010).

8. D. H. Erwin, J. W. Valentine, *The Cambrian Explosion: The Reconstruction of Animal Biodiversity* (Roberts & Co., ed. 1, 2013).

9. J. R. Wheeley, M. P. Smith, I. Boomer, Oxygen isotope variability in conodonts: Implications for reconstructing Palaeozoic palaeoclimates and palaeoceanography. *J. Geol. Soc.* **169**, 239–250 (2012).

10. A. J. Boucot, C. Xu, C. R. Scotese, R. J. Morley, *SEPM Concepts in Sedimentology and Paleontology. Phanerozoic Paleoclimate: An Atlas of Lithologic Indicators of Climate* (Society for Sedimentary Geology, ed. 1, 2013).

11. S. E. Peters, R. R. Gaines, Formation of the 'Great Unconformity' as a trigger for the Cambrian explosion. *Nature* **484**, 363–366 (2012).

12. S. M. Porter, Closing the phosphatization window: Testing for the influence of taphonomic megabias on the pattern of small shelly fossil decline. *PALAIOS* **19**, 178–183 (2004).

13. M. D. Brasier, Phosphogenic events and skeletal preservation across the Precambrian-Cambrian boundary interval. *Geol. Soc. Lond. Spec. Publ.* **52**, 289–303 (1990).

14. D. J. Siveter, M. Williams, D. Waloszek, A phosphatocopid crustacean with appendages from the Lower Cambrian. *Science* **293**, 474–479 (2001).

15. A. W. A. Rushton, The Cambrian of Wales and England, in *Cambrian of the British Isles, Norden and Spitzbergen*, C. H. Holland, Ed. (John Wiley & Sons Ltd, 1974), pp. 43–122.

16. T. H. Torsvik, L. R. M. Cocks, *Earth History and Palaeogeography* (Cambridge Univ. Press, 2016).

17. T. H. P. Harvey, M. Williams, D. J. Condon, P. R. Wilby, D. J. Siveter, A. W. A. Rushton, M. J. Leng, S. E. Gabbott, A refined chronology for the Cambrian succession of southern Britain. *J. Geol. Soc.* **168**, 705–716 (2011).

18. W. W. Schmahl, E. Griesshaber, C. Merkel, K. Kelm, J. Deuschle, R. D. Neuser, A. J. Götz, A. Sehrbrock, W. Mader, Hierarchical fibre composite structure and micromechanical properties of phosphatic and calcitic brachiopod shell biomaterials—An overview. *Mineral. Mag.* **72**, 541–562 (2008).

19. A. Williams, Shell structure, in *Treatise on Invertebrate Paleontology. Part H. Brachiopoda (Revised 1: Introduction)*, R. L. Kaesler, Ed. (Paleontological Institute, 1997), vol. 1.

20. Y. Kolodny, B. Luz, O. Navon, Oxygen isotope variations in phosphate of biogenic apatites, I. Fish bone apatite—Rechecking the rules of the game. *Earth Planet. Sci. Lett.* **64**, 398–404 (1983).

21. C. Lécuyer, P. Grandjean, C. C. Emig, Determination of oxygen isotope fractionation between water and phosphate from living lingulids: Potential application to palaeoenvironmental studies. *Palaeogeogr. Palaeoclim. Palaeoecol.* **126**, 101–108 (1996).

22. C. Lécuyer, R. Amiot, A. Touzeau, J. Trotter, Calibration of the phosphate $\delta^{18}O$ thermometer with carbonate–water oxygen isotope fractionation equations. *Chem. Geol.* **347**, 217–226 (2013).

23. P. N. Pearson, Oxygen isotopes in foraminifera: Overview and historical review, in *Reconstructing Earth's Deep Time Climate—The State of the Art in 2012, Paleontological Society Short Course, November 3, 2012. The Paleontological Society Papers* (The Paleontological Society, 2012), vol. 18, pp. 1–38.

24. R. T. Gregory, H. P. Taylor Jr., An oxygen isotope profile in a section of Cretaceous oceanic crust, Samail Ophiolite, Oman: Evidence for $\delta^{18}O$ buffering of the oceans by deep (>5 km) seawater-hydrothermal circulation at mid-ocean ridges. *J. Geophys. Res. Solid Earth* **86**, 2737–2755 (1981).

25. R. E. Came, J. M. Eiler, J. Veizer, K. Azmy, U. Brand, C. R. Weidman, Coupling of surface temperatures and atmospheric CO_2 concentrations during the Palaeozoic era. *Nature* **449**, 198–201 (2007).

26. S. Finnegan, K. Bergmann, J. M. Eiler, D. S. Jones, D. A. Fike, I. Eisenman, N. C. Hughes, A. K. Tripati, W. W. Fischer, The magnitude and duration of late Ordovician–early silurian glaciation. *Science* **331**, 903–906 (2011).

27. R. C. Cummins, S. Finnegan, D. A. Fike, J. M. Eiler, W. W. Fischer, Carbonate clumped isotope constraints on Silurian ocean temperature and seawater $\delta^{18}O$. *Geochim. Cosmochim. Acta* **140**, 241–258 (2014).

28. K. D. Bergmann, S. Finnegan, R. Creel, J. M. Eiler, N. C. Hughes, L. E. Popov, A paired apatite and calcite clumped isotope thermometry approach to estimating Cambro-Ordovician

seawater temperatures and isotopic composition. *Geochim. Cosmochim. Acta* **224**, 18–41 (2018).

29. A. Prokoph, G. A. Shields, J. Veizer, Compilation and time-series analysis of a marine carbonate $\delta^{18}O$, $\delta^{13}C$, $^{87}Sr/^{86}Sr$ and $\delta^{34}S$ database through Earth history. *Earth Sci. Rev.* **87**, 113–133 (2008).

30. P. S. Giles, Low-latitude Ordovician to Triassic brachiopod habitat temperatures (BHTs) determined from $\delta^{18}O_{[brachiopod\ calcite]}$: A cold hard look at ice-house tropical oceans. *Palaeogeogr. Palaeoclim. Palaeoecol.* **317–318**, 134–152 (2012).

31. J. F. Kasting, M. T. Howard, K. Wallmann, J. Veizer, G. Shields, J. Jaffrés, Paleoclimates, ocean depth, and the oxygen isotopic composition of seawater. *Earth Planet. Sci. Lett.* **252**, 82–93 (2006).

32. J. B. D. Jaffrés, G. A. Shields, K. Wallmann, The oxygen isotope evolution of seawater: A critical review of a long-standing controversy and an improved geological water cycle model for the past 3.4 billion years. *Earth Sci. Rev.* **83**, 83–122 (2007).

33. M. M. Joachimski, S. Breisig, W. Buggisch, J. A. Talent, R. Mawson, M. Gereke, J. R. Morrow, J. Day, K. Weddige, Devonian climate and reef evolution: Insights from oxygen isotopes in apatite. *Earth Planet. Sci. Lett.* **284**, 599–609 (2009).

34. A. N. LeGrande, G. A. Schmidt, Global gridded data set of the oxygen isotopic composition of seawater. *Geophys. Res. Lett.* **33**, L12604 (2006).

35. G. A. Schmidt, G. R. Bigg, E. J. Rohling, Global Seawater Oxygen-18 Database - v1.21 (1999);https://data.giss.nasa.gov/o18data/.

36. J. Tindall, R. Flecker, P. Valdes, D. N. Schmidt, P. Markwick, J. Harris, Modelling the oxygen isotope distribution of ancient seawater using a coupled ocean–atmosphere GCM: Implications for reconstructing early Eocene climate. *Earth Planet. Sci. Lett.* **292**, 265–273 (2010).

37. C. D. Roberts, A. N. LeGrande, A. K. Tripati, Sensitivity of seawater oxygen isotopes to climatic and tectonic boundary conditions in an early Paleogene simulation with GISS ModelE-R. *Paleoceanography* **26**, PA4203 (2011).

38. G. Suan, S.-M. Popescu, J.-P. Suc, J. Schnyder, S. Fauquette, F. Baudin, D. Yoon, K. Piepjohn, N. N. Sobolev, L. Labrousse, Subtropical climate conditions and mangrove growth in Arctic Siberia during the early Eocene. *Geology* **45**, 539–542 (2017).

39. C. L. O'Brien, S. A. Robinson, R. D. Pancost, J. S. S. Damsté, S. Schouten, D. J. Lunt, H. Alsenz, A. Bornemann, C. Bottini, S. C. Brassell, A. Farnsworth, A. Forster, B. T. Huber, G. N. Inglis, H. C. Jenkyns, C. Linnert, K. Littler, P. Markwick, N. E. Wrobel, Cretaceous sea-surface temperature evolution: Constraints from TEX$_{86}$ and planktonic foraminiferal oxygen isotopes. *Earth Sci. Rev.* **172**, 224–247 (2017).

40. J. Frieling, H. Gebhardt, M. Huber, O. A. Adekeye, S. O. Akande, G.-J. Reichart, J. J. Middelburg, S. Schouten, A. Sluijs, Extreme warmth and heat-stressed plankton in the tropics during the Paleocene-Eocene Thermal Maximum. *Sci. Adv.* **3**, e1600891 (2017).

41. D. Evans, N. Sagoo, W. Renema, L. J. Cotton, W. Müller, J. A. Todd, P. K. Saraswati, P. Stassen, M. Ziegler, P. N. Pearson, P. J. Valdes, H. P. Affek, Eocene greenhouse climate revealed by coupled clumped isotope–Mg/Ca thermometry. *Proc. Natl. Acad. Sci. U.S.A.* 201714744 (2018).

42. K. D. T. Nguyen, S. A. Morley, C.-H. Lai, M. S. Clark, K. S. Tan, A. E. Bates, L. S. Peck, Upper temperature limits of tropical marine ectotherms: Global warming implications. *PLOS ONE* **6**, e29340 (2011).

43. E. Nardin, Y. Goddéris, Y. Donnadieu, G. Le Hir, R. C. Blakey, E. Pucéat, M. Aretz, Modeling the early Paleozoic long-term climatic trend. *Geol. Soc. Am. Bull.* **123**, 1181–1192 (2011).

44. D. Avigad, A. Sandler, K. Kolodner, R. J. Stern, M. McWilliams, N. Miller, M. Beyth, Mass-production of Cambro–Ordovician quartz-rich sandstone as a consequence of chemical weathering of Pan-African terranes: Environmental implications. *Earth Planet. Sci. Lett.* **240**, 818–826 (2005).

45. M. Lindström, Cold age sediment in lower Cambrian of South Sweden. *Geol. Paleontol.* **6**, 9–23 (1972).

46. E. Landing, B. A. MacGabhann, First evidence for Cambrian glaciation provided by sections in Avalonian New Brunswick and Ireland: Additional data for Avalon–Gondwana separation by the earliest Palaeozoic. *Palaeogeogr. Palaeoclimatol. Palaeoecol.* **285**, 174–185 (2010).

47. R. L. Jacob, "Low frequency variability in a simulated atmosphere-ocean system," thesis, The University of Wisconsin (1997), 170 pp.

48. A. Pohl, Y. Donnadieu, G. Le Hir, J.-F. Buoncristiani, E. Vennin, Effect of the Ordovician paleogeography on the (in)stability of the climate. *Clim. Past* **10**, 2053–2066 (2014).

49. D. L. Royer, Y. Donnadieu, J. Park, J. Kowalczyk, Y. Goddéris, Error analysis of CO$_2$ and O$_2$ estimates from the long-term geochemical model GEOCARBSULF. *Am. J. Sci.* **314**, 1259–1283 (2014).

50. P. J. Brenchley, A. W. A. Rushton, M. Howells, R. Cave, Cambrian and Ordovician: The early Palaeozoic tectonostratigraphic evolution of the Welsh Basin, Midland and Monian Terranes of Eastern Avalonia, in *The Geology of England and Wales*, P. J. Brenchley, P. F. Rawson, Eds. (The Geological Society, ed. 2, 2006), pp. 25–74.

51. L. Jeppsson, R. Anehus, D. Fredholm, The optimal acetate buffered acetic acid technique for extracting phosphatic fossils. *J. Paleontol.* **73**, 964–972 (1999).

52. R. E. Blake, J. R. O'Neil, G. A. Garcia, Oxygen isotope systematics of biologically mediated reactions of phosphate: I. Microbial degradation of organophosphorus compounds. *Geochim. Cosmochim. Acta* **61**, 4411–4422 (1997).

53. J. R. O'Neil, L. J. Roe, E. Reinhard, R. E. Blake, A rapid and precise method of oxygen isotope analysis of biogenic phosphate. *Israel J. Earth Sci.* **43**, 203–212 (1994).

54. T. W. Vennemann, H. C. Fricke, R. E. Blake, J. R. O'Neil, A. Colman, Oxygen isotope analysis of phosphates: A comparison of techniques for analysis of Ag$_3$PO$_4$. *Chem. Geol.* **185**, 321–336 (2002).

55. C. J. Poulsen, R. L. Jacob, Factors that inhibit snowball Earth simulation. *Paleoceanography* **19**, PA4021 (2004).

56. Y. Donnadieu, Y. Goddéris, N. Bouttes, Exploring the climatic impact of the continental vegetation on the Mezosoic atmospheric CO$_2$ and climate history. *Clim. Past* **5**, 85–96 (2009).

57. T. H. Torsvik, L. R. M. Cocks, *BugPlates: Linking Biogeography and Palaeogeography* (Centre for Geodymanics, 2009); www.geodynamics.no.

58. D. O. Gough, Solar interior structure and luminosity variations. *Sol. Phys.* **74**, 21–34 (1981).

59. R. A. Berner, Inclusion of the weathering of volcanic rocks in the GEOCARBSULF model. *Am. J. Sci.* **306**, 295–302 (2006).

60. R. A. Locarnini, A. V. Mishonov, J. I. Antonov, T. P. Boyer, H. E. Garcia, O. K. Baranova, M. M. Zweng, C. R. Paver, J. R. Reagan, D. R. Johnson, M. Hamilton, D. Seidov, *World Ocean Atlas 2013, Volume 1: Temperature* (NOAA Atlas NESDIS, 2013).

61. M. R. Saltzman, E. Thomas, Carbon Isotope Stratigraphy, in *The Geologic Time Scale*, F. M. Gradstein, J. G. Ogg, M. D. Schmitz, G. M. Ogg, Eds. (Elsevier, 2012), pp. 207–232.

62. S. Peng, L. E. Babcock, R. A. Cooper, The Cambrian Period, in *The Geologic Time Scale*, F. M. Gradstein, J. G. Ogg, M. D. Schmitz, G. M. Ogg, Eds. (Elsevier, ed. 1, 2012), vol. 2, pp. 437–488.

63. B. Wenzel, C. Lécuyer, M. M. Joachimski, Comparing oxygen isotope records of silurian calcite and phosphate—$\delta^{18}O$ compositions of brachiopods and conodonts. *Geochim. Cosmochim. Acta* **64**, 1859–1872 (2000).

64. Y. Kolodny, B. Luz, Oxygen isotopes in phosphates of fossil fish; Devonian to Recent, in *Stable Isotope Geochemistry: A Tribute to Samuel Epstein*, H. P. Taylor Jr., J. R. O'Neil, I. R. Kaplan, Eds. (The Geochemical Society, Special Publication, 1991), pp. 105–119.

65. M. Barham, J. Murray, M. M. Joachimski, D. M. Williams, The onset of the Permo-Carboniferous glaciation: Reconciling global stratigraphic evidence with biogenic apatite $\delta^{18}O$ records in the late Visean. *J. Geol. Soc.* **169**, 119–122 (2012).

66. B. Chen, M. M. Joachimski, X.-d. Wang, S.-z. Shen, Y.-p. Qi, W.-k. Qie, Ice volume and paleoclimate history of the Late Paleozoic Ice Age from conodont apatite oxygen isotopes from Naqing (Guizhou, China). *Palaeogeogr. Palaeoclimatol. Palaeoecol.* **448**, 151–161 (2016).

67. M. M. Joachimski, P. H. von Bitter, W. Buggisch, Constraints on Pennsylvanian glacioeustatic sea-level changes using oxygen isotopes of conodont apatite. *Geology* **34**, 277–280 (2006).

68. S. I. Kaiser, T. Steuber, R. T. Becker, M. M. Joachimski, Geochemical evidence for major environmental change at the Devonian–Carboniferous boundary in the Carnic Alps and the Rhenish Massif. *Palaeogeogr. Palaeoclimatol. Palaeoecol.* **240**, 146–160 (2006).

69. C. Korte, H. W. Kozur, M. M. Joachimski, H. Strauss, J. Veizer, L. Schwark, Carbon, sulfur, oxygen and strontium isotope records, organic geochemistry and biostratigraphy across the Permian/Triassic boundary in Abadeh, Iran. *Int. J. Earth Sci.* **93**, 565–581 (2004).

70. J. Frieling, G.-J. Reichart, J. J. Middelburg, U. Röhl, T. Westerhold, S. M. Bohaty, A. Sluijs, Tropical Atlantic climate and ecosystem regime shifts during the Paleocene–Eocene Thermal Maximum. *Clim. Past* **14**, 39–55 (2018).

71. K. Littler, S. A. Robinson, P. R. Bown, A. J. Nederbragt, R. D. Pancost, High sea-surface temperatures during the Early Cretaceous Epoch. *Nat. Geosci.* **4**, 169–172 (2011).

72. A. Ando, B. T. Huber, K. G. MacLeod, D. K. Watkins, Early Cenomanian "hot greenhouse" revealed by oxygen isotope record of exceptionally well-preserved foraminifera from Tanzania. *Paleoceanography* **30**, 1556–1572 (2015).

73. A. Ando, B. T. Huber, K. G. MacLeod, T. Ohta, B.-K. Khim, Blake Nose stable isotopic evidence against the mid-Cenomanian glaciation hypothesis. *Geology* **37**, 451–454 (2009).

74. T. Aze, P. N. Pearson, A. J. Dickson, M. P. S. Badger, P. R. Bown, R. D. Pancost, S. J. Gibbs, B. T. Huber, M. J. Leng, A. L. Coe, A. S. Cohen, G. L. Foster, Extreme warming of tropical waters during the Paleocene–Eocene Thermal Maximum. *Geology* **42**, 739–742 (2014).

75. B. E. Bemis, H. J. Spero, J. Bijma, D. W. Lea, Reevaluation of the oxygen isotopic composition of planktonic foraminifera: Experimental results and revised paleotemperature equations. *Paleoceanography* **13**, 150–160 (1998).

76. K. L. Bice, R. D. Norris, Data Report: Stable Isotope Ratios of Foraminifers from ODP Leg 207, Sites 1257, 1258, and 1260, and a Cleaning Procedure for Foraminifers in Organic-Rich Shales (Ocean Drilling Program, 2005); www-odp.tamu.edu/publications/207_SR/104/104.htm.

77. K. L. Bice, B. T. Huber, R. D. Norris, Extreme polar warmth during the Cretaceous greenhouse? Paradox of the late Turonian $\delta^{18}O$ record at Deep Sea Drilling Project Site 511. *Paleoceanography* **18**, 1031 (2003).

78. P. K. Bijl, S. Schouten, A. Sluijs, G.-J. Reichart, J. C. Zachos, H. Brinkhuis, Early Palaeogene temperature evolution of the southwest Pacific Ocean. *Nature* **461**, 776–779 (2009).

79. A. Bornemann, R. D. Norris, O. Friedrich, B. Beckmann, S. Schouten, J. S. Damsté, J. Vogel, P. Hofmann, T. Wagner, Isotopic evidence for glaciation during the cretaceous supergreenhouse. *Science* **319**, 189–192 (2008).

80. P. Bown, P. Pearson, Calcareous plankton evolution and the Paleocene/Eocene thermal maximum event: New evidence from Tanzania. *Mar. Micropaleontol.* **71**, 60–70 (2009).

81. P. M. J. Douglas, H. P. Affek, L. C. Ivany, A. J. P. Houben, W. P. Sijp, A. Sluijs, S. Schouten, M. Pagani, Pronounced zonal heterogeneity in Eocene southern high-latitude sea surface temperatures. *Proc. Natl. Acad. Sci. U.S.A.* **111**, 6582–6587 (2014).

82. T. Dunkley Jones, D. J. Lunt, D. N. Schmidt, A. Ridgwell, A. Sluijs, P. J. Valdes, M. Maslin, Climate model and proxy data constraints on ocean warming across the Paleocene–Eocene Thermal Maximum. *Earth Sci. Rev.* **125**, 123–145 (2013).

83. F. Falzoni, M. R. Petrizzo, L. J. Clarke, K. G. MacLeod, H. C. Jenkyns, Long-term Late Cretaceous oxygen- and carbon-isotope trends and planktonic foraminiferal turnover: A new record from the southern midlatitudes. *Geol. Soc. Am. Bull.* **128**, 1725–1735 (2016).

84. S. Fauquette, J. Guiot, J.-P. Suc, A method for climatic reconstruction of the Mediterranean Pliocene using pollen data. *Palaeogeogr. Palaeoclimatol. Palaeoecol.* **144**, 183–201 (1998).

85. A. Forster, S. Schouten, M. Baas, J. S. Sinninghe Damsté, Mid-Cretaceous (Albian–Santonian) sea surface temperature record of the tropical Atlantic Ocean. *Geology* **35**, 919–922 (2007).

86. A. Forster, S. Schouten, K. Moriya, P. A. Wilson, J. S. Sinninghe Damsté, Tropical warming and intermittent cooling during the Cenomanian/Turonian oceanic anoxic event 2: Sea surface temperature records from the equatorial Atlantic. *Paleoceanography* **22**, PA1219 (2007).

87. O. Friedrich, J. Erbacher, K. Moriya, P. A. Wilson, H. Kuhnert, Warm saline intermediate waters in the Cretaceous tropical Atlantic Ocean. *Nat. Geosci.* **1**, 453–457 (2008).

88. J. Frieling, A. I. Iakovleva, G.-J. Reichart, G. N. Aleksandrova, Z. N. Gnibidenko, S. Schouten, A. Sluijs, Paleocene–Eocene warming and biotic response in the epicontinental West Siberian Sea. *Geology* **42**, 767–770 (2014).

89. C. J. Hollis, L. Handley, E. M. Crouch, H. E. G. Morgans, J. A. Baker, J. Creech, K. S. Collins, S. J. Gibbs, M. Huber, S. Schouten, J. C. Zachos, R. D. Pancost, Tropical sea temperatures in the high-latitude South Pacific during the Eocene. *Geology* **37**, 99–102 (2009).

90. C. J. Hollis, B. R. Hines, K. Littler, V. Villasante-Marcos, D. K. Kulhanek, C. P. Strong, J. C. Zachos, S. M. Eggins, L. Northcote, A. Phillips, The Paleocene–Eocene Thermal Maximum at DSDP Site 277, Campbell Plateau, southern Pacific Ocean. *Clim. Past* **11**, 1009–1025 (2015).

91. C. J. Hollis, K. W. R. Taylor, L. Handley, R. D. Pancost, M. Huber, J. B. Creech, B. R. Hines, E. M. Crouch, H. E. G. Morgans, J. S. Crampton, S. Gibbs, P. N. Pearson, J. C. Zachos, Early Paleogene temperature history of the Southwest Pacific Ocean: Reconciling proxies and models. *Earth Planet. Sci. Lett.* **349–350**, 53–66 (2012).

92. B. T. Huber, D. A. Hodell, C. P. Hamilton, Middle–Late Cretaceous climate of the southern high latitudes: Stable isotopic evidence for minimal equator-to-pole thermal gradients. *Geol. Soc. Am. Bull.* **107**, 1164–1191 (1995).

93. B. T. Huber, R. D. Norris, K. G. MacLeod, Deep-sea paleotemperature record of extreme warmth during the Cretaceous. *Geology* **30**, 123–126 (2002).

94. H. C. Jenkyns, L. Schouten-Huibers, S. Schouten, J. S. Sinninghe Damsté, Warm Middle Jurassic–Early Cretaceous high-latitude sea-surface temperatures from the Southern Ocean. *Clim. Past* **8**, 215–226 (2012).

95. C. M. John, S. M. Bohaty, J. C. Zachos, A. Sluijs, S. Gibbs, H. Brinkhuis, T. J. Bralower, North American continental margin records of the Paleocene-Eocene thermal maximum: Implications for global carbon and hydrological cycling. *Paleoceanography* **23**, PA2217 (2008).

96. C. R. Keating-Bitonti, L. C. Ivany, H. P. Affek, P. Douglas, S. D. Samson, Warm, not super-hot, temperatures in the early Eocene subtropics. *Geology* **39**, 771–774 (2011).

97. D. C. Kelly, T. J. Bralower, J. C. Zachos, Evolutionary consequences of the latest Paleocene thermal maximum for tropical planktonic foraminifera. *Palaeogeogr. Palaeoclimatol. Palaeoecol.* **141**, 139–161 (1998).

98. D. C. Kelly, T. J. Bralower, J. C. Zachos, I. P. Silva, E. Thomas, Rapid diversification of planktonic foraminifera in the tropical Pacific (ODP Site 865) during the late Paleocene thermal maximum. *Geology* **24**, 423–426 (1996).

99. J. P. Kennett, L. D. Stott, Abrupt deep-sea warming, palaeoceanographic changes and benthic extinctions at the end of the Palaeocene. *Nature* **353**, 225–229 (1991).

100. J.-H. Kim, J. van der Meer, S. Schouten, P. Helmke, V. Willmott, F. Sangiorgi, N. Koç, E. C. Hopmans, J. S. Sinninghe Damsté, New indices and calibrations derived from the distribution of crenarchaeal isoprenoid tetraether lipids: Implications for past sea surface temperature reconstructions. *Geochim. Cosmochim. Acta* **74**, 4639–4654 (2010).

101. S.-T. Kim, J. R. O'Neil, Equilibrium and nonequilibrium oxygen isotope effects in synthetic carbonates. *Geochim. Cosmochim. Acta* **61**, 3461–3475 (1997).

102. R. Kozdon, D. C. Kelly, N. T. Kita, J. H. Fournelle, J. W. Valley, Planktonic foraminiferal oxygen isotope analysis by ion microprobe technique suggests warm tropical sea surface temperatures during the Early Paleogene. *Paleoceanography* **26**, PA3206 (2011).

103. K. G. MacLeod, B. T. Huber, Á. J. Berrocoso, I. Wendler, A stable and hot Turonian without glacial $\delta^{18}O$ excursions is indicated by exquisitely preserved Tanzanian foraminifera. *Geology* **41**, 1083–1086 (2013).

104. K. Moriya, P. A. Wilson, O. Friedrich, J. Erbacher, H. Kawahata, Testing for ice sheets during the mid-Cretaceous greenhouse using glassy foraminiferal calcite from the mid-Cenomanian tropics on Demerara Rise. *Geology* **35**, 615–618 (2007).

105. P. N. Pearson, B. E. van Dongen, C. J. Nicholas, R. D. Pancost, S. Schouten, J. M. Singano, B. S. Wade, Stable warm tropical climate through the Eocene Epoch. *Geology* **35**, 211–214 (2007).

106. S. V. Petersen, D. P. Schrag, Antarctic ice growth before and after the Eocene-Oligocene transition: New estimates from clumped isotope paleothermometry. *Paleoceanography* **30**, 1305–1317 (2015).

107. M. R. Petrizzo, B. T. Huber, P. A. Wilson, K. G. MacLeod, Late Albian paleoceanography of the western subtropical North Atlantic. *Paleoceanography* **23**, PA1213 (2008).

108. P. L. Schoon, C. Heilmann-Clausen, B. P. Schultz, J. S. Sinninghe Damsté, S. Schouten, Warming and environmental changes in the eastern North Sea Basin during the Palaeocene–Eocene Thermal Maximum as revealed by biomarker lipids. *Org. Geochem.* **78**, 79–88 (2015).

109. S. Schouten, E. C. Hopmans, A. Forster, Y. van Breugel, M. M. M. Kuypers, J. S. Sinninghe Damsté, Extremely high sea-surface temperatures at low latitudes during the middle Cretaceous as revealed by archaeal membrane lipids. *Geology* **31**, 1069–1072 (2003).

110. J. S. Sinninghe Damsté, E. C. van Bentum, G.-J. Reichart, J. Pross, S. Schouten, A CO_2 decrease-driven cooling and increased latitudinal temperature gradient during the mid-Cretaceous Oceanic Anoxic Event 2. *Earth Planet. Sci. Lett.* **293**, 97–103 (2010).

111. A. Sluijs, P. K. Bijl, S. Schouten, U. Röhl, G.-J. Reichart, H. Brinkhuis, Southern ocean warming, sea level and hydrological change during the Paleocene-Eocene thermal maximum. *Clim. Past* **7**, 47–61 (2011).

112. A. Sluijs, H. Brinkhuis, S. Schouten, S. M. Bohaty, C. M. John, J. C. Zachos, G.-J. Reichart, J. S. Sinninghe Damsté, E. M. Crouch, G. R. Dickens, Environmental precursors to rapid light carbon injection at the Palaeocene/Eocene boundary. *Nature* **450**, 1218–1221 (2007).

113. A. Sluijs, S. Schouten, M. Pagani, M. Woltering, H. Brinkhuis, J. S. Sinninghe Damsté, G. R. Dickens, M. Huber, G.-J. Reichart, R. Stein, J. Matthiessen, L. J. Lourens, N. Pedentchouk, J. Backman, K. Moran; Expedition 302 Scientists, Subtropical Arctic Ocean temperatures during the Palaeocene/Eocene thermal maximum. *Nature* **441**, 610–613 (2006).

114. A. Sluijs, S. Schouten, T. H. Donders, P. L. Schoon, U. Röhl, G.-J. Reichart, F. Sangiorgi, J.-H. Kim, J. S. Sinninghe Damsté, H. Brinkhuis, Warm and wet conditions in the Arctic region during Eocene Thermal Maximum 2. *Nat. Geosci.* **2**, 777–780 (2009).

115. D. J. Thomas, T. J. Bralower, J. C. Zachos, New evidence for subtropical warming during the Late Paleocene thermal maximum: Stable isotopes from Deep Sea Drilling Project Site 527, Walvis Ridge. *Paleoceanography* **14**, 561–570 (1999).

116. D. J. Thomas, J. C. Zachos, T. J. Bralower, E. Thomas, S. Bohaty, Warming the fuel for the fire: Evidence for the thermal dissociation of methane hydrate during the Paleocene-Eocene thermal maximum. *Geology* **30**, 1067–1070 (2002).

117. A. K. Tripati, H. Elderfield, Abrupt hydrographic changes in the equatorial Pacific and subtropical Atlantic from foraminiferal Mg/Ca indicate greenhouse origin for the thermal maximum at the Paleocene-Eocene Boundary. *Geochem. Geophys. Geosyst.* **5**, Q02006 (2004).

118. N. A. G. M. van Helmond, A. Sluijs, G.-J. Reichart, J. S. Sinninghe Damsté, C. P. Slomp, H. Brinkhuis, A perturbed hydrological cycle during Oceanic Anoxic Event 2. *Geology* **42**, 123–126 (2014).

119. N. A. G. M. van Helmond, A. Sluijs, J. S. Sinninghe Damsté, G.-J. Reichart, S. Voigt, J. Erbacher, J. Pross, H. Brinkhuis, Freshwater discharge controlled deposition of Cenomanian–Turonian black shales on the NW European epicontinental shelf (Wunstorf, northern Germany). *Clim. Past* **11**, 495–508 (2015).

120. T. Yamaguchi, R. D. Norris, No place to retreat: Heavy extinction and delayed recovery on a Pacific guyot during the Paleocene–Eocene Thermal Maximum. *Geology* **43**, 443–446 (2015).

121. S. Zaarur, H. P. Affek, M. T. Brandon, A revised calibration of the clumped isotope thermometer. *Earth Planet. Sci. Lett.* **382**, 47–57 (2013).

122. J. C. Zachos, S. Schouten, S. Bohaty, T. Quattlebaum, A. Sluijs, H. Brinkhuis, S. J. Gibbs, T. J. Bralower, Extreme warming of mid-latitude coastal ocean during the Paleocene-Eocene Thermal Maximum: Inferences from TEX86 and isotope data. *Geology* **34**, 737–740 (2006).

123. J. C. Zachos, M. W. Wara, S. Bohaty, M. L. Delaney, M. R. Petrizzo, A. Brill, T. J. Bralower, I. Premoli-Silva, A transient rise in tropical sea surface temperature during the paleocene-eocene thermal maximum. *Science* **302**, 1551–1554 (2003).

124. J. C. Zachos, L. D. Stott, K. C. Lohmann, Evolution of Early Cenozoic marine temperatures. *Paleoceanography* **9**, 353–387 (1994).

Citation: T. W. Hearing, T. H. P. Harvey, M. Williams, M. J. Leng, A. L. Lamb, P. R. Wilby, S. E. Gabbott, A. Pohl, Y. Donnadieu, An early Cambrian greenhouse climate. *Sci. Adv.* **4**, eaar5690 (2018).

Science Advances

An early Cambrian greenhouse climate

Thomas W. HearingThomas H. P. HarveyMark WilliamsMelanie J. LengAngela L. LambPhilip R. WilbySarah E. GabbottAlexandre PohlYannick Donnadieu

View the article online
https://www.science.org/doi/10.1126/sciadv.aar5690
Permissions
https://www.science.org/help/reprints-and-permissions